RSC Advances

PAPER

View Article Online
View Journal | View Issue

Cite this: *RSC Adv.*, 2017, **7**, 2025

New melilite $(Ca,Sr,Ba)_4MgAl_2Si_3O_{14}:Eu^{2+}$ phosphor: structural and spectroscopic analysis for application in white LEDs

Ha Jun Kim,†[a] Sanjith Unithrattil,†[a] Yoon Hwa Kim,[a] Woon Jin Chung[b] and Won Bin Im*[a]

Received 4th November 2016
Accepted 15th December 2016

DOI: 10.1039/c6ra26317h

www.rsc.org/advances

A series of new Eu^{2+}-activated melilite-structured phosphor compounds was developed through solid-state reactions. The structural and spectroscopic properties of the phosphors were analyzed; all phosphors showed emissions in the blue to green regions of visible light. All developed compounds showed asymmetric broad-bands with shoulders on the lower-energy sides. The spectroscopic parameters of Eu^{2+} emission in the host compound were estimated and their correlation with the chemical composition of the phosphor was verified. The luminescence mechanism in the phosphors was analyzed through luminescence decay measurements. The broad emission band in the developed compound, due to transitions in the $4f^6 5d–4f^7$ levels of Eu^{2+}, was found to be ideal for application in solid-state lighting devices. The feasibility of the compound as a potential white LED phosphor was demonstrated by fabricating a white LED with excellent emission properties.

Introduction

In the history of electrically driven illuminant devices, starting with the incandescent lamp commercialized by Thomas Edison, rapid improvements in technology have occurred in successive intervals. With the discovery of blue light-emitting diodes (LEDs) by Nakamura *et al.*, lighting technology has reached a point at which the parameters remaining for improvement are considerably fewer.[1–3] In present white-light technology, in which a blue LED is combined with a broad-band emitting phosphor, the efficiency of the LED chip is approaching unity.

The development of an ideal phosphor covering the entire visible region of the spectrum is an ongoing process. Certain phosphors are widely used because they show superior emission properties. $Y_3Al_5O_{12}:Ce^{3+}$ (YAG:Ce^{3+}) is one of the most prominent; however, it has drawbacks that must be addressed for white LEDs (wLEDs) to replace all conventional illumination sources.[4–6] The important drawbacks to address include the low color rendering index and thermal instability of luminescence properties. In recent years, several alternative phosphors have been proposed,[7,8] but a breakthrough has not yet occurred.

Researchers have followed different strategies to develop a new phosphor meeting all criteria required of the intended material. One widely followed strategy is to alter the properties of existing phosphors through substitutions of suitable elements. Although this strategy shows promise, the extent of alteration is often limited by the inherent properties of the phosphor lattice, which limits the amounts of the substituent atom that can be accommodated. Desirable changes in the properties of the material typically require substantial amounts of the substituent elements, unless the substituting species are used as dopants. Barring certain structures with inherent tolerance for large-scale substitution, most crystal lattices accommodate only low percentages of substituent elements.[8–10] The identification of substitution-friendly structures is crucial in such strategies. Most such structures are of mineral origin.

Melilite is a mineral group found in high-temperature metamorphosed impure limestone and silica-undersaturated igneous rocks. Melilite compounds crystallize with tetragonal symmetry and have many applications, ranging from optical materials to fuel cell ingredients.[11] The tetragonal structure of the melilite compounds can accommodate different ions through substitutions and cosubstitutions. This property of the structure has been widely utilized in achieving optical materials of desired properties.[12,13] In this study, we have developed a series of new broadband-emitting phosphors utilizing the substitutability of melilite-structured compounds. Based on industrial requirements, a broadband-emitting green phosphor was materialized. The structural and optical properties of the compounds and the correlations of atomic composition with the phosphor emission properties were analyzed through X-ray

[a]*School of Materials Science and Engineering, Optoelectronics Convergence Research Center, Chonnam National University, 300 Yongbong-dong, Buk-gu, Gwangju, 500-757, Republic of Korea. E-mail: imwonbin@jnu.ac.kr; Fax: +82-62-530-1699; Tel: +82-62-530-1715*

[b]*Institute for Rare Metals & Division of Advanced Materials Engineering, Kongju National University, Cheonan, Chungnam 330-717, South Korea*

† Authors contributed equally to this work.

diffraction (XRD) and discussed thoroughly. The feasibility of the tested compounds as potential green-emitting components in solid-state lighting was demonstrated by fabricating wLEDs.

Results and discussion

Structural properties

Melilite minerals are tetragonally structured sorosilicate compounds formed from solid solutions of various endmembers. The compounds crystallize in the $P\bar{4}2_1m$ space group with two formula units per unit cell. The basic formula of these compounds is represented by the general structure $A_2B(C_2O_7)$, where A is a major cation such as Na^+, Ca^{2+}, Sr^{2+}, Ba^{2+}, La^{3+}, or Y^{3+}; B is Mg^{2+}, Fe^{2+}, or Al^{3+}; and C is typically a minor cation like Si^{4+}, Al^{3+}, or B^{3+}. The overall structure has three kinds of oxygen polyhedra formed by the A, B, and C cations. The A cation at 4e forms the distorted dodecahedron AO_8, an isolated tetrahedron BO_4 is formed by B cations at 2a sites, and a smaller tetrahedron CO_4 formed by C cations at 4e sites. CO_4 tetrahedra exist in pairs, effectively forming C_2O_7 di-ortho groups.[14] Three crystallographically distinct oxygen atoms occupy the 2c, 4e, and 8f sites. All tetrahedral units are connected in two dimensions along the (001) plane, forming $(T_3O_7)^{n-}$ layers, where T includes both B and C cations. These layers are interlinked by the cations positioned between them.[11] The effective formal charge n of the T_3O_7 units varies in different compounds, with usual values of 3, 4, or 5. In $(Ba,Sr,Ca)_4MgAl_2Si_3O_{14}$, the dodecahedron is occupied by the alkaline earth elements (Ba, Sr, and Ca), while the larger tetrahedron is shared by the divalent Mg^{2+} and trivalent Al^{3+}. Three-quarters of the smaller tetrahedra are occupied by Si^{4+}, while the remainder contains Al^{3+}. Fig. 1 shows the unit cell representation of the structure, along with the dodecahedral, tetrahedral, and di-ortho groups.

In $Sr_2Ca_2MgAl_2Si_3O_{14}$ (SCMAS), where all divalent ions in the major cation layer are alkaline earth elements, the dopant Eu^{2+} ions are expected to occupy these tetrahedral sites because of the similarity in ionic radii. The bonding nature of these sites is primarily determined by the major cations, which determine the interatomic spacing between cations and the O^{2-} anions. For a broadband-emitting activator like Eu^{2+} in SCMAS, the emission peak position and the spectral width of the bands are determined by the bonding parameters and the polarizability of the chain-forming cations arranged in alternating layers. In SCMAS, these cations include Mg^{2+}, Al^{3+}, and Si^{4+}, which ensure diversity in the bonding nature. This diversity is crucial for tuning the emission of such compounds.

The diversity in the nature of the bonding anions causes a non-spherical distribution of electron density around the major cation site where the activator ion is likely to be occupied. As discussed in the preceding section, this asymmetry arises from the dissimilarity of ions occupying the 4e sites of the structure, which are coordinated to the polyhedra and di-ortho units containing further dissimilar ions, *viz.* Mg^{2+}, Al^{3+}, and Si^{4+}. Notably, although the 4e sites are occupied by divalent cations with different ionic radii, the polarizing tetrahedral units with electrons shared by the major cations are of diverse oxidation states, and the polyanion units bear different formal charges. These differently charged units have different polarizability levels, which determine the availability of electrons in bond formation. This causes the non-spherical charge density distribution around major cation sites. The relevant bonding

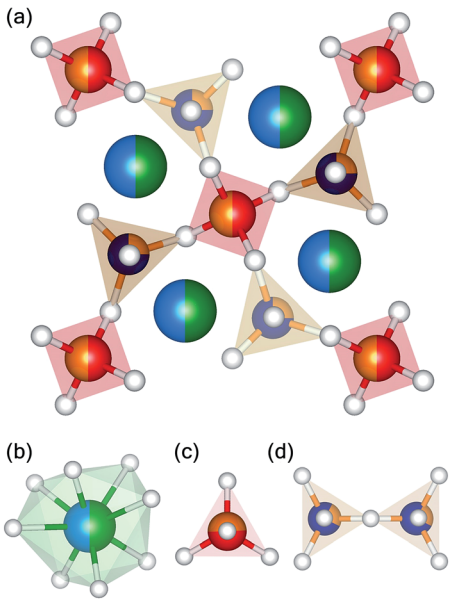

Fig. 1 (a) Unit cell representation of $Sr_2Ca_2MgAl_2Si_3O_{14}$, and the (b) dodecahedral, (c) tetrahedral, and (d) di-ortho units in the unit cell of the melilite structure. Blue, green, red, orange, violet, and white spheres indicate Sr, Ca, Mg, Si, Al, and O atoms, respectively.

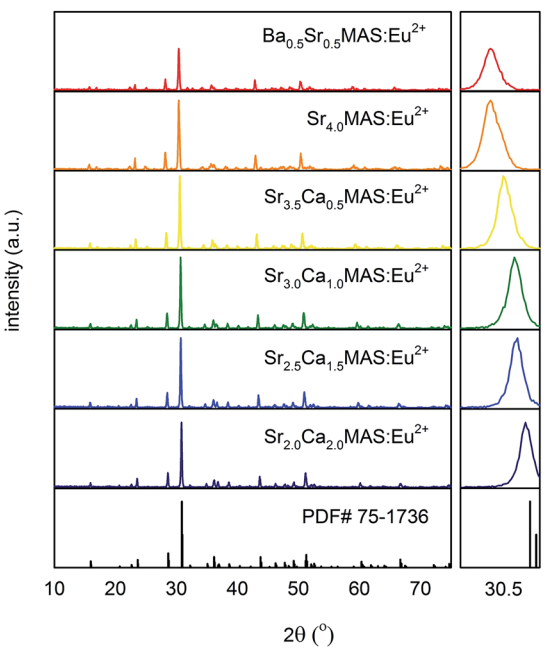

Fig. 2 XRD profiles of $(Ba,Sr,Ca)_4MgAl_2Si_3O_{14}$ with different ratios of alkaline earth ions substituted in the structure, compared to reference pattern. Panel on the right depicts the XRD phase evolution at ~30.5° with increasing substitution of larger cations.

parameters are estimated by the Rietveld refinement of the structure.

Fig. 2 shows the XRD profile of the compounds $A_4MgAl_2Si_3O_{14}:Eu^{2+}$ ($A_4MAS:Eu^{2+}$), where A is the alkaline earth elements Ca, Sr, and Ba, respectively, in different substitutional ratios and in increasing order of atomic radii. A starting composition of $(Sr_2Ca_2)MAS:Eu^{2+}$ was chosen. The ratio of major cations in these sites was subsequently replaced with those of higher ionic radii from the same group, and compositions up to $(Ba_{0.5}Sr_{3.5})MAS:Eu^{2+}$ were obtained. XRD profiles of all samples are comparable to the reference pattern PDF# 75-1736, indicating that the compounds each form a single phase. The change in XRD profiles of the changing compounds is shown in the right panel of Fig. 2, where successive peaks at 30.5° are shifted to 30° by increasing the ionic radius of the substituent, as is expected.

Fig. 3 shows the Rietveld refinement of the XRD profile of the selected composition, $SCMAS:Eu^{2+}$, using a pseudo-Voigt profile function. The structural model of $CaYAl_3O_7$, as reported by Park *et al.*,[15] was used as the starting model. The lattice positions of the elements were assigned based on the relative ionic radii of the cations occupying the respective sites. The refinement was converged until the R_p, R_{wp}, and the goodness-of-fit parameter (χ^2) were in acceptable ranges, indicating phase formation. The refinement parameters of the selected composition are tabulated in Table 1.

Fig. 4 shows the evolution in the unit cell parameters (a) *a*, *b*, and (b) *c*, and (c) the unit cell volume, *V*, obtained from the Le Bail method[16] with corresponding values tabulated in Table 2. The increasing substitution of the larger cation Sr^{2+} for Ca^{2+} in the selected composition $SCMAS:Eu^{2+}$ correlates to a linear increase in the lattice parameters, which is proportional to the amount of the substituent component. The linear fit of the lattice parameters of the compound, barring $BaSMAS:Eu^{2+}$ in which the substituent ion is Ba^{2+}, have linear fitting factors of 0.989, 0.959, and 0.999, indicating that the compounds obey Vegard's law[17] for lattice parameters in the cation-substituted compounds. This suggests isostructural phase formation in the compound series.

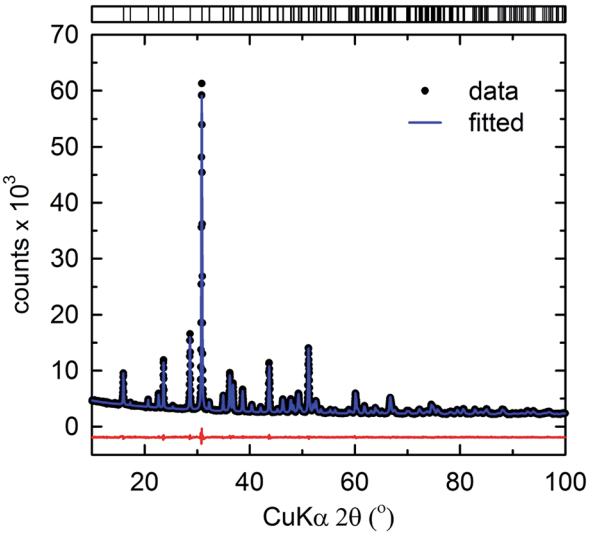

Fig. 3 Rietveld refinement of the powder XRD profile of $Sr_2Ca_2MgAl_2Si_3O_{14}$. Data (points) and fit (lines), the difference profile, and expected reflection positions are displayed.

Table 1 Rietveld refinement of $Sr_2Ca_2MgAl_2Si_3O_{14}:Eu^{2+}$ numbers in parentheses are the estimated standard deviations of the least significant figure

Formula	$Sr_2Ca_2MgAl_2Si_3O_{14}:Eu^{2+}$
Radiation type	X-ray
2θ range/degree	10–100
T/K	295
Symmetry	Tetragonal
Space group	$P\bar{4}2_1m$
Z	1
a, *b*/Å	7.8415(1)
c/Å	5.1318(1)
Volume/Å^3	315.55(0)
R_p/%	2.07
R_{wp}/%	2.71
χ^2	1.80

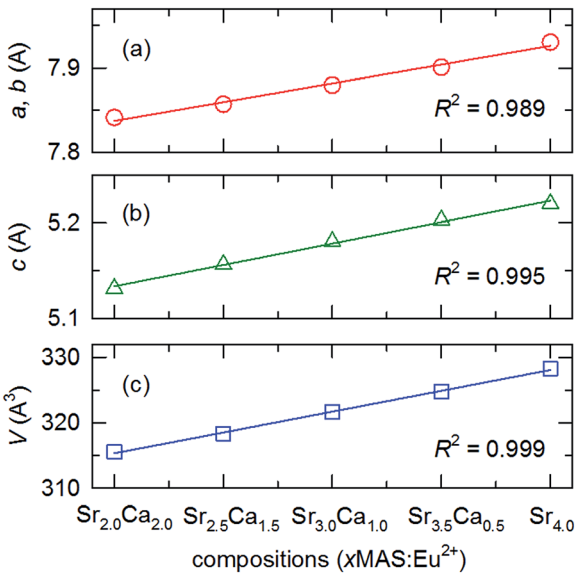

Fig. 4 Variation in lattice parameters (a) *a*, *b*, (b) *c*, and (c) *V* in $SCMAS:Eu^{2+}$ with variations in cationic ratio. Linear fits of data points corresponding to the Ca^{2+}–Sr^{2+} pair are shown in each plot.

Table 2 Lattice parameters of the compound series obtained from XRD patterns using the Le Bail method. Numbers in parentheses are the estimated standard deviations of the least significant figure

Phosphor	*a*, *b*/Å	*c*/Å	*V*/Å^3
$Sr_{2.0}Ca_{2.0}MAS:Eu^{2+}$	7.8415(1)	5.1318(1)	315.55(0)
$Sr_{2.5}Ca_{1.5}MAS:Eu^{2+}$	7.8572(1)	5.1568(1)	318.36(0)
$Sr_{3.0}Ca_{1.0}MAS:Eu^{2+}$	7.8797(1)	5.1808(1)	321.67(1)
$Sr_{3.5}Ca_{0.5}MAS:Eu^{2+}$	7.9007(1)	5.2031(1)	324.78(1)
$Sr_4MAS:Eu^{2+}$	7.9304(3)	5.2201(3)	328.30(2)
$Ba_{0.5}Sr_{3.5}MAS:Eu^{2+}$	7.9418(2)	5.2426(2)	330.66(1)

Luminescence properties

Fig. 5(a) and (b) show the PL excitation and emission bands of the compositions, respectively, as functions of the substituent element levels. All PL excitation bands exhibit broad bands from ~270 to ~450 nm, originating from the f–d transitions in the Eu^{2+} ions. The dependence of the PLE spectra on the composition of the tetragonal structure is noticeable. The normalized PLE spectra show that the peak excitation of the Eu^{2+} activator in the compounds remains characteristically similar in all compounds, except for $Ba_{0.5}$SAMS:Eu^{2+}. In $Ba_{0.5}$SAMS:Eu^{2+}, the excitation peak in the high-energy region is positioned at ~320 nm, while in all other compounds it is positioned at ~360 nm. The excitation peak in the lower-energy region lies in the range of 420 to 430 nm in all compositions. The excitation band edge experiences a progressive red shift with increases in the concentration of the smaller-radius ions.

The normalized emission spectra of the compounds, shown in Fig. 5(b), depict broadband emissions with shoulders on the lower-energy sides. This is not characteristic of the emission band originating from the $4f^6$5d–$4f^7$ transition in Eu^{2+} ions. When considering the feature, as well as the fact that the compound has only one crystallographic site for substituting the activator, which is the eight-coordinated dodecahedral 4e site, the shoulder can be interpreted as a consequence of random substitution by activator ions at these crystallographic sites, which are typically occupied by diverse cations, *viz.* Ba^{2+}, Sr^{2+}, and Ca^{2+}. These different cations have different ionic radii and bonding parameters; as a result, the corresponding sites and the adjacent sites are affected by local distortions. This affects the average distance of the metal ligands, which is important in determining the emission peak position through the crystal field effect. The crystal-field splitting parameters $10Dq$ of the compositions were estimated by identifying the center of gravity of the t_{2g} and e_g transitions; the corresponding values are tabulated in Table 3. Crystal field splitting is significantly decreased with increases in the average cation size. This agrees with theoretical expectations, as the average distance between Eu^{2+} and O^{2-} is considerably smaller in Ba^{2+}-substituted compounds than in non-substituted counterparts. The distorted dodecahedral site occupied by the activator ion deviates from cubic symmetry, and the crystal field varies accordingly.[14] Thus, the lattice sites of the activator ion, though crystallographically similar, attain different symmetries; therefore, the overall emission shows a lower-energy-side shoulder.

The emission spectra of the compounds also progressively shift towards the red region with substitution of smaller cations. This may be attributed to the change in centroid shift, which is the average energy of the 5d-orbitals of the excitation levels. This energy is independent of the shape and symmetry of the coordination polyhedron in which the activator ion is occupied. However, centroid shift is influenced by the nature of the ligands surrounding the central cation. Considering that the lower and higher band edges of the excitation spectrum also shift with the peak emission wavelength in a similar pattern, the emission shift may originate from the centroid shift in the $4f^6$5d^1 excitation levels of Eu^{2+}. This is expressed as the average of the shift in the $4f^6$5d^1 levels relative to the free ion value. For the SCMAS host in which Eu^{2+} occupies the eightfold coordination sites, the centroid shift can be estimated from the following equation:[18]

$$\varepsilon_c = E_c(2+,\ \text{free}) - \left(E(2+,\ \text{A}) + 0.37 + \frac{\varepsilon_{cfs}(2+,\ \text{A})}{r(\text{A})}\right)\ \text{eV} \quad (1)$$

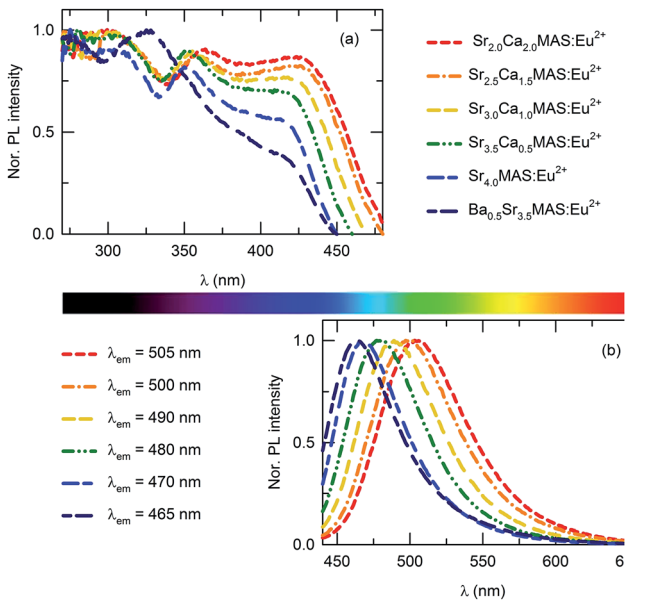

Fig. 5 (a) PL excitation and (b) emission spectra of $(Ba,Sr,Ca)_4MgAl_2Si_3O_{14}$ with variations in the major cation ratio.

Table 3 Peak energy of the $4f^7$–$4f^6[^7F_0]5d^1$ excitation transition [E(2+, A)], peak energy of emission band [E^{em}], full width at half peak intensity of the emission band [I^{em}], red shift (D(2+, A)), crystal field splitting ($10Dq$), centroid shift [ε_c], energy of the zero-phonon line [E^{ZPL}], and Stokes shift [ΔS] expressed in cm^{-1} at room temperature

Phosphor	E(2+, A)	E^{em}	I^{em}	D(2+, A)	$10Dq$	ε_c	E^{ZPL}	ΔS
$Sr_{2.0}Ca_{2.0}$MAS:Eu^{2+}	23 419	19 881	2722	10 617	10 945	6793	21 459	3538
$Sr_{2.5}Ca_{1.5}$MAS:Eu^{2+}	23 529	20 121	2718	10 507	10 485	6959	21 668	3408
$Sr_{3.0}Ca_{1.0}$MAS:Eu^{2+}	23 640	20 534	2677	10 396	10 258	6984	22 075	3106
$Sr_{3.5}Ca_{0.5}$MAS:Eu^{2+}	23 923	20 964	2636	10 113	9410	7210	22 471	2959
Sr_4MAS:Eu^{2+}	24 213	21 368	2460	9823	8900	7226	22 883	2845
$Ba_{0.5}Sr_{3.5}$MAS:Eu^{2+}	24 272	21 598	2545	9764	7175	8202	23 201	2674

as proposed by Dorenbos. Here, $E_c(2+, A)$ is the barycenter energy of the high spin level in free Eu^{2+}, taken as 4.93 eV; $E(2+, A)$ is the peak energy of the excitation transition; 0.37 eV is the difference between $E(2+, A)$ and the barycenter energy of the first $4f^6[^7F]5d^1$ band in the spectrum; $\varepsilon_{cfs}(2+, A)$ is the crystal field splitting; and $r(A)$ assumes the value 5/3 for eightfold symmetry sites. The obtained values of ε_c, along with the relevant parameters, are tabulated in Table 3. A centroid shift varying between 0.84 and 1.02 eV is observed in the compound series. This primarily occurs because of the diversity in the polarizing-cation tetrahedra with which the ligand of the central cations is shared. The non-identical nature of the central cation's neighbors induces a larger centroid shift, evident from the calculated values of ε_c. In addition, adjusting the central cation could alter the relative distribution of the neighboring cations. The diverse polarizing cations, *viz.* Mg^{2+}, Al^{3+}, and Si^{4+}, together share the two lattice sites 2a and 4e. These cations should occupy the designated sites in a random distribution, so that the effective charge on each ligand is determined by the polarizability of the central cation in the ligand. Barring Mg^{2+}, which occupies only the larger isolated tetrahedron, Al^{3+} and Si^{4+} can occupy both the isolated tetrahedron and di-ortho units because of their ionic radii.

The redshift $D(2+, A)$ of the Eu^{2+} $4f^65d^1$ electronic configuration is the sum of the centroid shift and the crystal field splitting. This can be estimated from the relation[18]

$$D(2+, A) = E_0(2+, \text{free}) - E(2+, A) \quad (2)$$

where $E_0(2+, \text{free})$ is the difference in energy between the ground state and the lowest excited level in free Eu^{2+} (4.22 eV) and $E(2+, A)$ is the peak energy of the Eu^{2+} $4f^7$–$4f^6[^7F_0]5d^1$ excitation transition. The calculated values of $D(2+, A)$ are tabulated in Table 2. The redshift decreases with increases in the concentration of cations of larger radii in the host lattice. However, this decrease is not as rapid as that in the crystal field parameter $10Dq$, as a corresponding increase in the centroid shift somewhat nullifies the redshift. Thus, it is confirmed that adjusting the cations by maintaining the ratio of polarizing cation species can cause significant reordering in the bonding parameters of the structure near the cation. The diversity in the emission centers of the structure on introduction of major cations can also be understood from the variation in full width at half maximum (Γ^{em}) of the phosphors. In general, the Γ^{em} of emission bands are significantly influenced by the difference between emission centers. The lowest value (2460 cm^{-1}) of Γ^{em} among the compositional series was obtained for $Sr_4MAS:Eu^{2+}$ phosphor which contains only one kind of major cation. In all the other analyzed phosphors, irrespective of the size of the additionally introduced cations, Γ^{em} increased.

To clarify the understanding of the emission mechanisms of the phosphors with different cation contents, the luminescence decay profiles of the compounds were analyzed. The decay profiles of the compounds were fitted with a three-component exponential decay model:

$$I = a\,e^{-t/\tau'} + b\,e^{-t/\tau''} + c\,e^{-t/\tau'''} \quad (3)$$

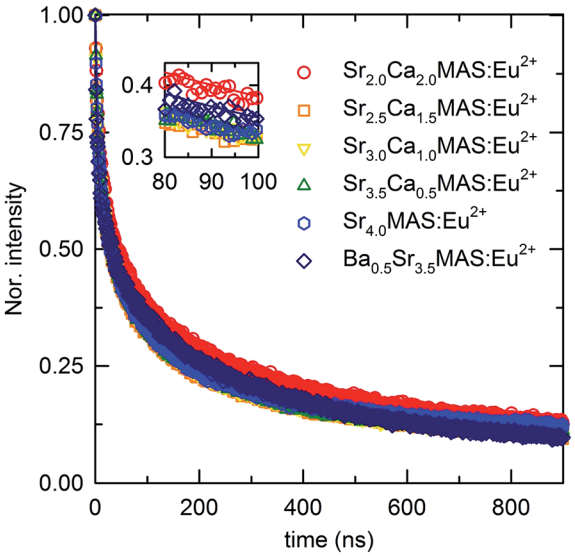

Fig. 6 Luminescence decay profile of $(Ba,Sr,Ca)_4MgAl_2Si_3O_{14}$ with variations in the major cation ratio, fitted with three-component exponential decay model. Inset shows the magnified view in 80 to 100 ns region.

where I is the PL intensity at a given time t; τ', τ'', and τ''' are the exponential components, respectively; and a, b, and c are constants. Fig. 6 shows the decay profile of the compositions fitted with the corresponding theoretical model and Table 4 lists the fitting parameters.

The decay profiles of the compounds have faster and slower components. The slowest decay component, identified by the decay constant τ''' of $\sim 10^3$ ns, indicates an origin in the non-electronic levels; in other words, long-lasting phosphorescence originates from the recombination of trapped electrons. The contribution of intrinsic trap levels to long-lasting luminescence was widely reported in previous studies on melilite-structured compounds.[19] The variation in the decay constant of the slower component among different compounds indicates the difference in trap depths among the compositions. The two relatively faster components, evidently originating from the Eu^{2+} decay process, indicate two types of emission centers in the structure. In a structure having only one crystallographically distinct Eu^{2+} site, this indicates diversity in the lattice parameters arising from the random substitution of the different types

Table 4 The luminescence decay parameters of the SCMAS:Eu^{2+} phosphors obtained from the three-component exponential decay model

Phosphor	a	τ'/ns	b	τ''/ns	c	τ'''/ns
$Sr_{2.0}Ca_{2.0}MAS:Eu^{2+}$	0.346	90.91	0.361	6.94	0.293	1.03×10^3
$Sr_{2.5}Ca_{1.5}MAS:Eu^{2+}$	0.355	90.91	0.416	7.19	0.229	1.06×10^3
$Sr_{3.0}Ca_{1.0}MAS:Eu^{2+}$	0.362	90.91	0.402	6.62	0.236	1.05×10^3
$Sr_{3.5}Ca_{0.5}MAS:Eu^{2+}$	0.371	90.91	0.403	7.09	0.226	1.12×10^3
$Sr_4MAS:Eu^{2+}$	0.371	90.91	0.402	6.45	0.226	1.33×10^3
$Ba_{0.5}Sr_{3.5}MAS:Eu^{2+}$	0.324	90.91	0.391	3.95	0.285	1.00×10^3

of polarizing cations in the two crystallographically distinct sites of the structure. The component τ' has a constant value for the entire sample series, suggesting that one type of emission center is identical throughout the compositional series. Meanwhile, the component τ'' varies in different compositions, which can be attributed to the distortion of emission centers by extensive substitution. The luminescence lifetimes of the phosphor compositions, moving from a 1 : 1 ratio of Sr^{2+} and Ca^{2+} to a 1 : 7 ratio of Ba^{2+} and Sr^{2+}, have no regular trend, confirming the randomness of the substitutions, which is also evident from the multi-component emission bands. As explained in the preceding section, the introduction of diverse cations to the major cation site, along with the diversity of the polarizing cations distributed randomly in the unit cell, induces multiple emission levels because of the difference in the centroid shifts among activator ions substituted at different crystallographic positions. The presence of additional pathways for the luminescence decay process is known to negatively affect the average lifetimes of the excited levels. These additional pathways are created by the additional and repositioned levels in the band structures of the substituted compounds. The distortions in existing emission centers also contribute to the decay process.

In a multi-phosphor converted wLED configuration using a blue or near-UV excitation source, a phosphor that covers the green region of the visible spectrum is of utmost importance. An efficient phosphor with an emission band in this region often provides higher luminous efficacy when used in combination with broadband-emitting orange-red phosphors. Therefore, we chose to further optimize the green-emitting SCMAS:Eu^{2+} for potential applications. Fig. 7(a), (b) and (c) show the PL excitation and emission spectra of the selected composition, peak emission wavelength, and relative intensity of the phosphor, respectively, as functions of the activator concentration. The optimum activator concentration of the selected composition is 0.02 mole content; this compound has a peak emission wavelength of 505 nm. The emission peak position of the compound experiences a redshift with increases in the activator concentration. The emission peak position shifts from 502 to 512 nm as the concentration is increased from 0.01 to 0.05 mole content. This red-shift in the emission peak is due to the reabsorption of Eu^{2+} emission. The probability of such reabsorption increases with decreases in the average separation between emission centers, because of the increased concentration.

In order to investigate the concentration-related quenching phenomenon of the phosphor, the critical distance between activator ions was estimated using a relation proposed by Blasse:[20]

$$R_c \approx 2\left[\frac{3V}{4\pi X_c N}\right]^{1/3} \quad (4)$$

where V is the unit cell volume, N the number of total Eu^{2+} sites per unit cell, and X_c the critical concentration, defined as the activator concentration at which quenching begins. For SCMAS:Eu^{2+}, V, N, and X_c are 314.70 Å^3, 1, and 0.02, respectively.

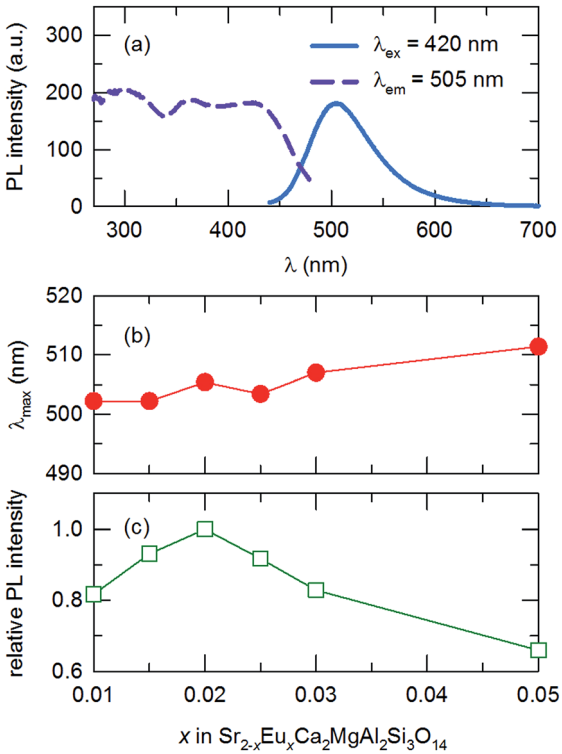

Fig. 7 (a) PL excitation and emission spectra of the optimized compound $Sr_{1.98}Ca_2Eu_{0.02}MgAl_2Si_3O_{14}$, (b) peak emission wavelength, (c) relative emission intensity of the compound as a function of the activator concentration x, and (d) the log–log plot of the intensity per activator ion against activator ion concentration.

The critical distance of energy transfer R_c is calculated as 31 Å. In order to understand the mechanism behind the concentration quenching, the relation[21]

$$\frac{1}{x} = \frac{k}{1+\beta(x)^{\theta/3}} \quad (5)$$

was used, in which k and β are constants and θ assumes the values of 6, 8, and 10 for dipole–dipole, dipole-quadrupole, and quadrupole–quadrupole interactions, respectively. Fig. 7(d) shows the $\log(I/x)$ *vs.* $\log(x)$ plot from eqn (5); the slope of the linear fit, given by $-\theta/3$, is identified as ~1.5. The lower θ value of 4.5 indicates that dipole–dipole interactions among the Eu^{2+} emission centers on the (002) plane is the concentration quenching mechanism. The possibility of such interactions among the Eu^{2+} emission centers located on the next cation plane with those of the same layer is equally possible, as the interatomic separation in this direction is both equal to the lattice parameter of the structure and much smaller than the critical distance estimated above.

Prototype wLEDs were fabricated to determine the feasibility of the optimized compound as a component in solid-state lighting devices. The phosphor, along with a yellow-emitting YAG:Ce^{3+} (Force4 Corp.) phosphor and red-emitting K_2SiF_6:Mn^{4+} (KSF:Mn^{4+}) (Force4 Corp.), were taken in 6 : 3 : 1 ratio in combination with a blue-emitting LED, was prepared. Fig. 8(a) shows the EL spectra of the fabricated wLED under

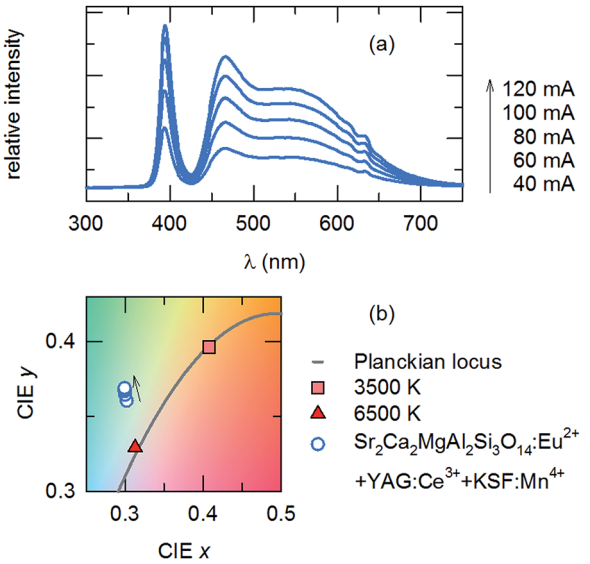

Fig. 8 (a) Luminescence of the InGaN LED + phosphor, under different forward bias currents (indicated): InGaN (λ_{max} = 395 nm) + $Sr_2Ca_2MgAl_2Si_3O_{14}:Eu^{2+}$ + yellow + red phosphor. Inset: digital photograph of the fabricated wLED with and without applying driving voltage. (b) CIE chromatic coordinates of the device under different forward bias currents. The Planckian locus line and points corresponding to color temperatures of 3500 K and 6500 K are indicated.

various forward bias current values. The corresponding Commission Internationale de l'Eclairage (CIE) chromaticity coordinates from the devices are shown in Fig. 8(b). The luminescence intensity of the phosphor combinations is increased with increases in the forward bias current, indicating the absence of saturation. The wLEDs provided a cold white light with the CIE color coordinate of (0.36, 0.30) under a bias current of 20 mA. The corresponding correlated color temperature (CCT) was 6542 K and the color rendering index (CRI) was 96. This confirms that the developed phosphor is a viable candidate material for applications in solid-state lighting devices.

Experimental

Powder samples of $(Ba,Sr,Ca)_4MgAl_2Si_3O_{14}:Eu^{2+}$ were prepared by a solid-state reaction from the starting materials of $SrCO_3$ (Aldrich, 99.9%), $CaCO_3$ (Aldrich, 99.9%), $BaCO_3$ (Aldrich, 99.9%), SiO_2 (Aldrich, 99.9%), MgO (Aldrich, 99.9%), Al_2O_3 (Aldrich, 99.99%), and Eu_2O_3 (Aldrich, 99.99%). The as-received raw materials were weighed and thoroughly mixed together using an agate mortar and pestle with acetone as the dispersing medium. The powder was dried and heated at various temperatures between 1300 and 1400 °C. The activator ions were reduced by a constant flow of 5%/95% H_2/N_2 gases. The furnace heating was set to occur over 4 h; samples were maintained at high temperature for 4 h before being naturally cooled to room temperature. The obtained phosphor cakes were then ground into fine powder and analyzed.

The phase formations of all prepared phosphor samples were determined by analyzing the XRD data obtained from Cu Kα radiation (Philips X'Pert diffractometer) over the angular range $10° \leq 2\theta \leq 100°$ with a step size of 0.026°. Rietveld refinement was performed on the obtained data with the GSAS[22] using a pseudo-Voigt profile function. The luminescence properties of the samples were investigated using room-temperature photoluminescence (PL) spectra measured on a Hitachi F-4500 fluorescence spectrophotometer over the wavelength range of 200–650 nm. Fluorescence decay curves were measured using a 374 nm pulsed laser diode on a spectrometer at the KAIST, Daejon, South Korea.

Conclusions

The structural and luminescence properties of broadband-emitting compounds with the general formula $(Ba,Sr,Ca)_4MgAl_2Si_3O_{14}$ were studied. The spectroscopic parameters of the compounds were identified and the effects of cationic substituents with different ionic radii on the host crystals were established. The centroid shift of the emission levels varied from 6793 to 8202 cm^{-1}, with a corresponding variation in Stokes shift of 3538 to 2674 cm^{-1} on increasing the concentration of larger cations. The broad emission of the compound, arising from transitions in the Eu^{2+} $4f^65d$–$4f^7$ levels, experienced a redshift with decreases in the ionic radii of the cationic elements, by which tuning of the emission band was achieved. The wLEDs fabricated using the optimized phosphor, commercial yellow and red phosphors, and a near-UV LED showed excellent color properties, with a CRI of 96.

Acknowledgements

This research was supported by the Strategic Key-Material Development and the Materials and Components Research and Development bodies, funded by the Ministry of Knowledge Economy (MKE, Korea). This work was also financially supported by the Basic Science Research Program through the National Research Foundation of Korea (NRF) funded by the Ministry of Science, ICT & Future Planning (NRF-2014R1A1A1002909, 2016R1E1A2020571).

Notes and references

1 S. Nakamura, *MRS Bull.*, 2009, **34**, 101–107.
2 Q.-Q. Zhu, L. Wang, N. Hirosaki, L. Y. Hao, X. Xu and R.-J. Xie, *Chem. Mater.*, 2016, **28**, 4829–4839.
3 C. Zhang, T. Uchikoshi, R.-J. Xie, L. Liu, Y. Cho, Y. Sakka, N. Hirosaki and T. Sekiguchi, *J. Mater. Chem. C*, 2015, **3**, 7642–7651.
4 S. Nishiura, S. Tanabe, K. Fujioka and Y. Fujimoto, *Opt. Mater.*, 2011, **33**, 688–691.
5 W. B. Im, H. S. Yoo, S. Vaidyanathan, K. H. Kwon, H. J. Park, Y. I. Kim and D. Y. Jeon, *Mater. Chem. Phys.*, 2009, **115**, 161–164.
6 J. L. Leaño, S.-Y. Lin, A. Lazarowska, S. Mahlik, M. Grinberg, C. Liang, W. Zhou, M. S. Molokeev, V. V. Atuchin, Y.-T. Tsai, C. C. Lin, H.-S. Sheu and R.-S. Liu, *Chem. Mater.*, 2016, **28**, 6822–6825.

7 Y. Liu, *et al.*, Research on trend of worldwide white LED phosphors technologies and market development, *12th China International Forum on Solid State Lighting (SSLCHINA)*, Shenzhen, 2015, pp. 33–39.
8 H. Zhou, Q. Wang and Y. Jin, *J. Mater. Chem. C*, 2015, **3**, 11151–11162.
9 W. B. Im, N. George, J. Kurzman, S. Brinkley, A. Mikhailovsky, J. Hu, B. F. Chmelka, S. P. DenBaars and R. Seshadri, *Adv. Mater.*, 2011, **23**, 2300–2305.
10 H. Ji, L. Wang, Y. Cho, N. Hirosaki, M. S. Molokeev, Z. Xia, Z. Huang and R.-J. Xie, *J. Mater. Chem. C*, 2016, **4**, 9872–9878.
11 X. Kuang, M. A. Green, H. Niu, P. Zajdel, C. Dickinson, J. B. Claridge, L. Jantsky and M. J. Rosseinsky, *Nat. Mater.*, 2008, **7**, 498–504.
12 Z. Xia and Q. Liu, *Prog. Mater. Sci.*, 2016, **84**, 59–117.
13 Z. Xia, C. Ma, M. S. Molokeev, Q. Liu, K. Rickert and K. R. Poeppelmeier, *J. Am. Chem. Soc.*, 2015, **137**, 12494–12497.
14 E. I. Givargizov, A. Melnikova and D. W. Wester, *Growth of crystals*, Springer, 1986.
15 S. H. Park, K. H. Lee, S. Unithrattil, H. S. Yoon, H. G. Jang and W. B. Im, *J. Phys. Chem. C*, 2012, **116**, 26850–26856.
16 C. Lartigue, A. Le Bail and A. Percheron-Guegan, *J. Less-Common Met.*, 1987, **129**, 65–76.
17 A. R. Denton and N. W. Ashcroft, *Phys. Rev. A*, 1991, **43**, 3161.
18 P. Dorenbos, *J. Phys.: Condens. Matter*, 2003, **15**, 4797.
19 I. P. Sahu, D. Bisen, N. Brahme and M. Ganjir, *Luminescence*, 2015, **30**, 1318–1325.
20 S. J. Kim, H. S. Jang, S. Unithrattil, Y. H. Kim and W. B. Im, *J. Am. Ceram. Soc.*, 2016, **99**, 557–563.
21 Z. Xia, H. Liu, X. Li and C. Liu, *Dalton Trans.*, 2013, **42**, 16588–16595.
22 A. C. Larson and R. B. Von Dreele, *Los Alamos Natl. Lab., [Rep.] LA (U. S.)*, 1994, 86–748.